The white matter fiber tract deforms most in the perpendicular direction during *in vivo* volunteer impacts

Zhou Zhou,[1*] Christoffer Olsson,[2] T. Christian Gasser,[3] Xiaogai Li,[1] Svein Kleiven[1]

[1] Division of Neuronic Engineering, KTH Royal Institute of Technology, Stockholm, 14152, Sweden.

[2] Division of Biomedical Imaging, KTH Royal Institute of Technology, Stockholm, 14152, Sweden.

[3] Material and Structural Mechanics, Department of Engineering Mechanics, KTH Royal Institute of Technology, Stockholm, 14152, Sweden.

[*] Corresponding author. Email: zhouz@kth.se

Abstract

White matter (WM) tract-related strains are increasingly used to quantify brain mechanical responses, but their dynamics in live human brains during *in vivo* impact conditions remain largely unknown. Existing research primarily looked into the normal strain along the WM fiber tracts (i.e., tract-oriented normal strain), but it is rarely the case in reality that the fiber tract only endures tract-oriented normal strain. In this study, we aim to extend the measurement of WM deformation by quantifying the normal strain perpendicular to the fiber tract (i.e., tract-perpendicular normal strain) and the shear strain along and perpendicular to the fiber tract (i.e., tract-oriented shear strain and tract-perpendicular shear strain, respectively). To achieve this, we combine the three-dimensional strain tensor from the tagged magnetic resonance imaging (tMRI) with the diffuse tensor imaging (DTI) from an open-access dataset, including 44 volunteer impacts under neck rotations (N = 30, peak angular acceleration: 228.6 ± 8.3 rad/s^2) and neck extensions (N = 14, peak angular acceleration: 185.5 ± 59.2 rad/s^2). The strain tensor is rotated to the coordinate system with one axis aligned with DTI-revealed fiber orientation and then four tract-related strain measures are calculated. The results show that tract-perpendicular normal strain peaks are the largest among the four strain types and tract-oriented normal strains are the lowest. The peak values for tract-oriented normal strain, tract-perpendicular normal strain, tract-oriented shear strain, and tract-perpendicular shear strain are 0.020 ± 0.005, 0.028 ± 0.007, 0.024 ± 0.006 and 0.023 ± 0.006 under the neck rotation, and 0.013 ± 0.002, 0.019 ± 0.004, 0.016 ± 0.003, and 0.017 ± 0.003 under the neck extension, respectively. The distribution of tract-related strains is affected by the head loading mode. Our study presents a comprehensive *in vivo* strain quantification towards a multifaceted understanding of WM dynamics. For the first time, we find the WM fiber tract deforms most in the perpendicular direction, illuminating new fundamental of brain mechanics. The reported strain results can be used to evaluate the biofidelity of computational head models, especially those intended to predict brain strains under non-injurious conditions.

Keywords

Volunteer head impacts, tagged magnetic resonance imaging, diffusion tensor imaging, tract-related deformation, in vivo white matter deformation

Highlights

- We combine multimodal imaging analyses with continuum mechanics to quantify *in vivo* white matter tract-related deformation.
- We present three-dimensional, full-field normal and shear strains along and perpendicular to the white matter fiber tracts in 44 volunteer impacts.
- We find the white matter fiber tract deforms most in the perpendicular direction.

List of abbreviations

tMRI	tagged magnetic resonance imaging
DTI	diffusion tensor imaging
TBI	traumatic brain injury
WM	white matter

Introduction

Traumatic brain injury (TBI) is a pressing public health and socio-economic problem. Annually, around 69 million people worldwide suffer a TBI [1]. In Europe, about 7.7 million people live with TBI-induced disability, incurring immense personal suffering and huge economic costs [2]. In Sweden, the annual number of TBI-related emergency department visits is estimated to be 30,000 with 10,000 requiring hospitalization [3]. Despite substantial efforts to reduce the occurrence and mitigate the severity, TBI remains to be the leading cause of death in young adults and its incidence is alarmingly increasing in the elderly [4]. There is a clear need for more research to address this TBI-related epidemic, of which how the brain responds during impacts is the central requestion to be answered.

Various approaches are used to elucidate the biomechanical fundamentals behind brain trauma. In *in situ* cadaveric tests, the post-mortem human subjects are meticulously instrumented to measure brain responses with the impact severity close to the traumatic level [5]. For example, Hardy and colleagues [6, 7] conducted 35 cadaveric tests with blunt impacts to track the motion of 12 sparse makers within the deep brain region, which was later analysed to estimate the brain strain [8, 9] and strain rate [10]. More recently, Alshareef, et al. [11] instrumented six head-neck complexes, each of which equipped 24 markers throughout the brain parenchyma, to obtain brain motion in 72 impacts with pure rotational loadings. *In vitro* models play a crucial role in comprehending the mechanobiological cascades of TBI, especially at the cellular and subcellular level, by relating controlled mechanical inputs to the resultant morphological damage or electrical dysfunction of experimental tissues [12, 13]. For example, Morrison III and colleagues mechanically injured *in vitro* cultured rat hippocampi. It was found that the cell death was monotonically dependent on the strain [14], while the functional tolerance was affected by strain and strain rate in a complex fashion [15]. *In silico* head models are increasingly used to quantitatively simulate the localized tissue response during head impacts [16, 17]. Modern *in silico* models feature subject-specific geometry [18, 19], anisotropic and heterogeneous brain material [20-22], and fluid representation of the cerebrospinal fluid [23, 24]. Encouraging correlations have been reported between the response of the *in silico* model and experimentally quantified histology or clinically diagnosed injury [25-28].

Another important line to study human brain biomechanics is *in vivo* quantitative imaging, which can offer complementary information of the intracranial dynamics under non-injurious conditions [29]. Today, many *in vivo* imaging modalities (e.g., magnetic resonance elastography [30, 31], amplified magnetic resonance imaging (MRI) [32], and phase-contrast MRI [33]) are used to enlighten the mechanics of the well-hidden brain under volunteer impacts or physiological conditions, of which the tagged MRI (tMRI) is particularly illuminating. tMRI is an imaging technique that was originally developed to measure cardiovascular deformation [34]. In 2005, Bayly, et al. [35] pioneeringly implemented tMRI to image brain deformation under sub-injurious occipital impacts. Over the past two

decades, tMRI has been applied to measure brain responses in diverse voluntary scenarios (e.g., axial rotation [36], frontal impact [37]) with multiple technical advancements to improve imaging efficacy, accuracy, and resolution [38-41]. In 2021, Bayly, et al. [42] established an open-access dataset, including tMRI-recorded brain responses from 50 volunteer tests and other pertinent information (e.g., impact kinematics, structure imaging of volunteers).

Axonal injury is a frequent form of trauma in the white matter (WM) and characterized by diffuse lesions within the fiber tracts usually consisting of oriented axons. Given this pathologic feature, there has been growing interest in quantifying the loading endured by the fiber tract [43]. For *in vivo* experimental data, only one study [44] calculated the normal strain along the fiber tracts (i.e., tract-oriented normal strain) by projecting the tMRI-recorded brain strain tensor along the primary fiber direction estimated from the diffusion tensor imaging (DTI) in 20 volunteer impacts (10 neck rotations and 10 neck extensions). It is worth clarifying the tract-oriented normal strain is alternatively termed as fiber strain [45], tract-oriented strain [46], and axonal strain [45, 47] in the literature. Despite interesting results, the tract-oriented normal strain only represents one aspect of fiber deformation. Considering the complexity of impact loading and the tensorial nature of the strain, it is rarely the case in reality that the fiber only endures the tract-oriented normal strain during impacts. A multifaceted quantification of fiber deformation remains to be performed.

The current study aims to present a comprehensive quantification of WM tract-related deformation under volunteer impacts. To this end, the tMRI-recorded brain strain tensor data in 44 volunteer tests is related to the DTI-derived fiber direction. Through this, we quantify the normal strain and shear strain along and perpendicular to the fiber tract. This investigation finds the WM tract deforms most in the perpendicular direction, unravelling new fundamental of brain mechanics. The reported strain data can be used to evaluate the biofidelity of *in silico* models.

Methods

Volunteer tests and imaging data

The brain strain tensor data during volunteer tests and brain imaging are acquired from a publicly available dataset where details regarding study approval, subject recruitment, test protocol, imaging acquisition, and processing are available elsewhere [42]. Briefly, the volunteer was rapidly rotated at non-injurious levels by a custom-built neck rotation device (rotation within the axial plane along the inferior-superior axis) or neck extension device (rotation within the sagittal plane about the left-right axis). The angular kinematics within the primary rotating plane were recorded, i.e., the axial plane for the neck rotation (Fig 1A) and the sagittal plane for the neck extension (Fig 1B). In each test, three-dimensional (3D), full-field, time-varying brain strain tensor, including six independent components (Fig 1C), were measured using tMRI at a spatial resolution of 1.5 mm or 2.0 mm and a temporal resolution of 18 ms, 19.5 ms and 20 ms. These subject-specific tensorial brain strain data under known

head loading conditions were further complemented by multimodal structural imaging data of the same subject. As the WM is the structure of interest in the current study, DTI and brain segmentation are particularly relevant. DTI is an imaging technique in which the anisotropic movement of water molecules within the brain is utilized to estimate the WM fiber tracts. In the dataset, DTI-derived information, including the principal eigenvector of the diffusion tensor and the fraction anisotropy (FA) map (Fig 1D), were available. The brain was segmented into different anatomical structures (Fig 1E), of which the WM region included cerebral WM, cerebellar WM, and brainstem. For each test, the structural images were processed with the same spatial resolutions as the tMRI.

In the current study, 44 volunteer tests are included to estimate the WM tract-related strains. Note that, from the 50 tests in the original dataset, 4 tests performed on cadavers and 2 tests without DTI are excluded. These 44 tests, including 30 neck rotations and 14 neck extensions, were acquired from 38 subjects (20 male, 18 female) with an average age of 31.7 ± 10.8 years (range: 19-59 years). Structural imaging data (e.g., brain segmentation, DTI, and its derivatives) are spatially aligned with the tMRI-derived brain strain tensor data, except for 4 tests of which co-registrations between different imaging modalities are performed by ourselves, with the use of common neuroimaging tools from the FMRIB Software Library [48, 49].

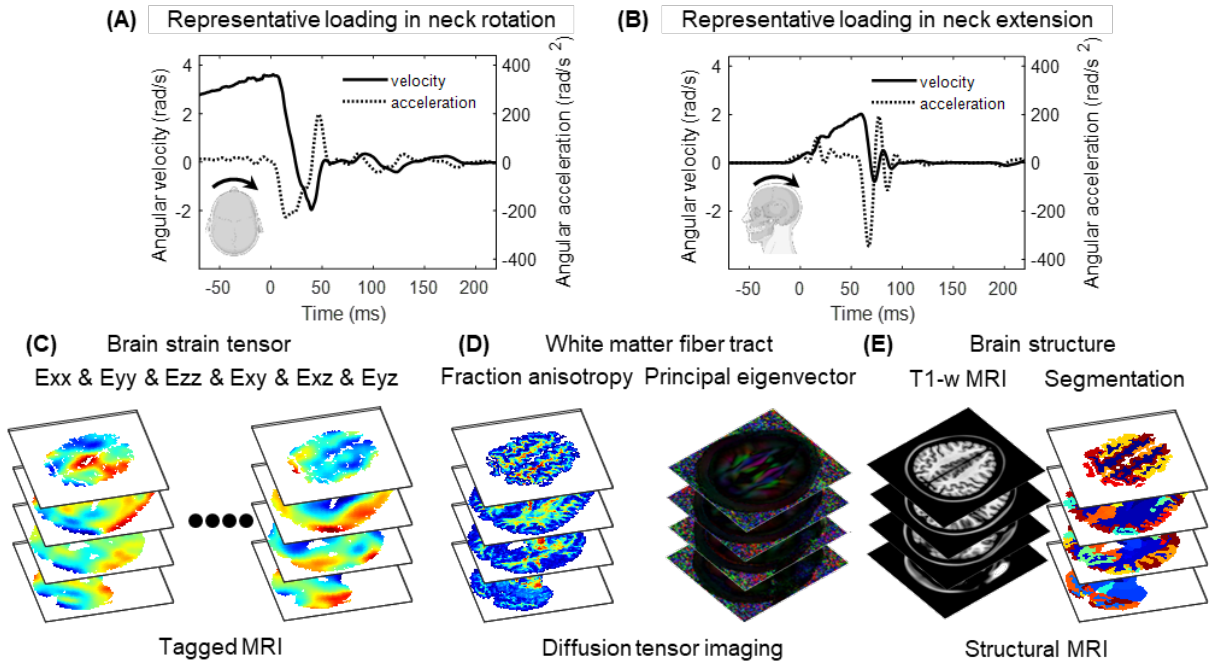

Fig 1. Voluntary tests in neck rotation and neck extension and imaging acquisition. (A) Angular kinematics in the axial plane for one representative neck rotation test. (B) Angular kinematics in the sagittal plane for one representative neck extension test. (C) 3D full-field, time-varying Green-Lagrange brain strain tensor measured by tagged MRI. (D) White matter fiber-related information (i.e., fractional anisotropy, and principal eigenvector quantifying the primary direction of fiber tracts) derived from diffusion tensor imaging. (E) Brain structure and segmentation. Note that the kinematics in subfigures A and B correspond to the two impacts that are used as representative tests for illustration purposes in the "Results" section.

Computation of white matter tract-related strains

To calculate the WM tract-related deformation, the tMRI-derived brain strain tensor is rotated to the coordinate system with one axis aligned with the DTI-derived fiber orientation, through which the components in the transformed tensor quantify multiple strain modes endured by the fiber (Fig 2). This calculation is applied to all WM voxels (i.e., voxels with FA values ≥ 0.2), of which the fiber orientation is approximated as the first principal eigenvector of the diffusion tensor. In each time frame of tMRI, we calculate the tract-oriented normal strain (ε_a), a metric that has also been chosen as the parameter of interest in one early *in vivo* study [44]. As a step further, we also study three new tract-related strains, including tract-perpendicular normal strain (ε_t, the maximal normal strain perpendicular to the fiber tract), tract-oriented shear strain (γ_a, the shear strain along the fiber tract), and tract-perpendicular shear strain (γ_t, the maximal shear strain perpendicular to the fiber tract). As the strain components change when going around the fiber tract, ε_t and γ_t represent their maximum values. This calculation is performed at each time frame of the tMRI. The mathematical derivation of tract-related strains is detailed in Appendix A.

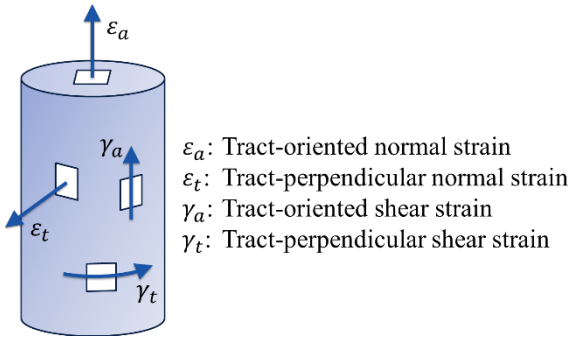

Fig 2. Sketch of four tract-related strains characterizing the normal strain and shear strain along and perpendicular to the fiber tract.

Statistical analysis

For the four tract-related strains, we identify the peak values accumulated over time during the two head loading protocols (i.e., neck rotation and neck extension). This is motivated since the time-accumulated strain peaks are often used for injury analysis [50, 51]. It is also a compromised strategy to address the disparity of temporal resolution in tMRI (30 tests with a time resolution of 18 ms vs. 3 tests with a time resolution of 19.5 ms vs. 11 tests with a time resolution of 20 ms). For the spatial resolution disparity of tMRI (31 tests with a voxel resolution of 1.5 mm vs. 13 tests with a voxel resolution of 2 mm), its influence on the tract-related strains remains negligible, see Appendix B. Hence, strain results with different spatial resolutions are combined for the statistical analysis.

For each test, the peak tract-related strains are computed for three WM subregions (i.e., cerebral WM, cerebellar WM, brainstem) and the whole WM. To avoid potential artifacts, the 95th percentile peak values are reported, the same strategy as in previous studies [44, 52]. To compare the magnitudes of different strain types (non-normally distributed), Wilcoxon matched-pairs signed-rank tests are performed for all four types of tract-related strain peaks at the cerebral WM, cerebellar WM, brainstem,

and whole WM. To assess the influence of head loading mode (i.e., neck rotation and neck extension) on the fiber deformation, Mann-Whitney U tests are conducted on four tract-related strain peaks (non-normally distributed). Within each head loading mode, we perform Pearson's correlations to test the dependence between the maximum tract-related strains and two angular kinematic peaks (i.e., peak change in angular velocity and peak angular acceleration). The threshold for significance is $p < 0.05$.

Results

At the individual level, tract-related strain responses in one specific subject, who performed both neck rotation and neck extension, are reported in Fig 3 as illustrative cases. The peak change in angular velocity and peak angular acceleration are 5.6 rad/s and 226.8 rad/s^2 for neck rotation (Fig 1A), and 2.8 rad/s and 345.6 rad/s^2 for neck extension (Fig 1B). Spatially heterogeneous strain patterns are noted in the WM and the regions with high strains (i.e., areas in red in Fig 3A and Fig 3C) are dependent on the head loading mode and strain type. For neck rotation, high tract-oriented normal and shear strains are sparsely distributed and mostly occur at the boundary of cerebral WM and periventricular region, while high tract-perpendicular normal and shear strains exhibit relatively continuous patterns that extend from the anterior-superior site in the left cerebrum to the deep region in the right cerebrum (Fig 3A). In the neck extension, high tract-oriented normal strain is primarily noted in the brainstem, while high tract-perpendicular normal and shear strains, tract-oriented shear strain appear isolated and occur mostly in the anterior-superior cerebral region (primarily close to the midsagittal plane), inferior cerebellar area, and brainstem (Fig 3C). Interestingly, left-right symmetric strain patterns with respect to the midsagittal plane are noted in neck extension, but not in neck rotation. For the strain peak in the neck rotation (Fig 3C) and neck extension (Fig 3D), the largest value is consistently noted in tract-perpendicular normal strain across all examined regions (i.e., cerebral WM, cerebellar WM, brainstem, and whole WM).

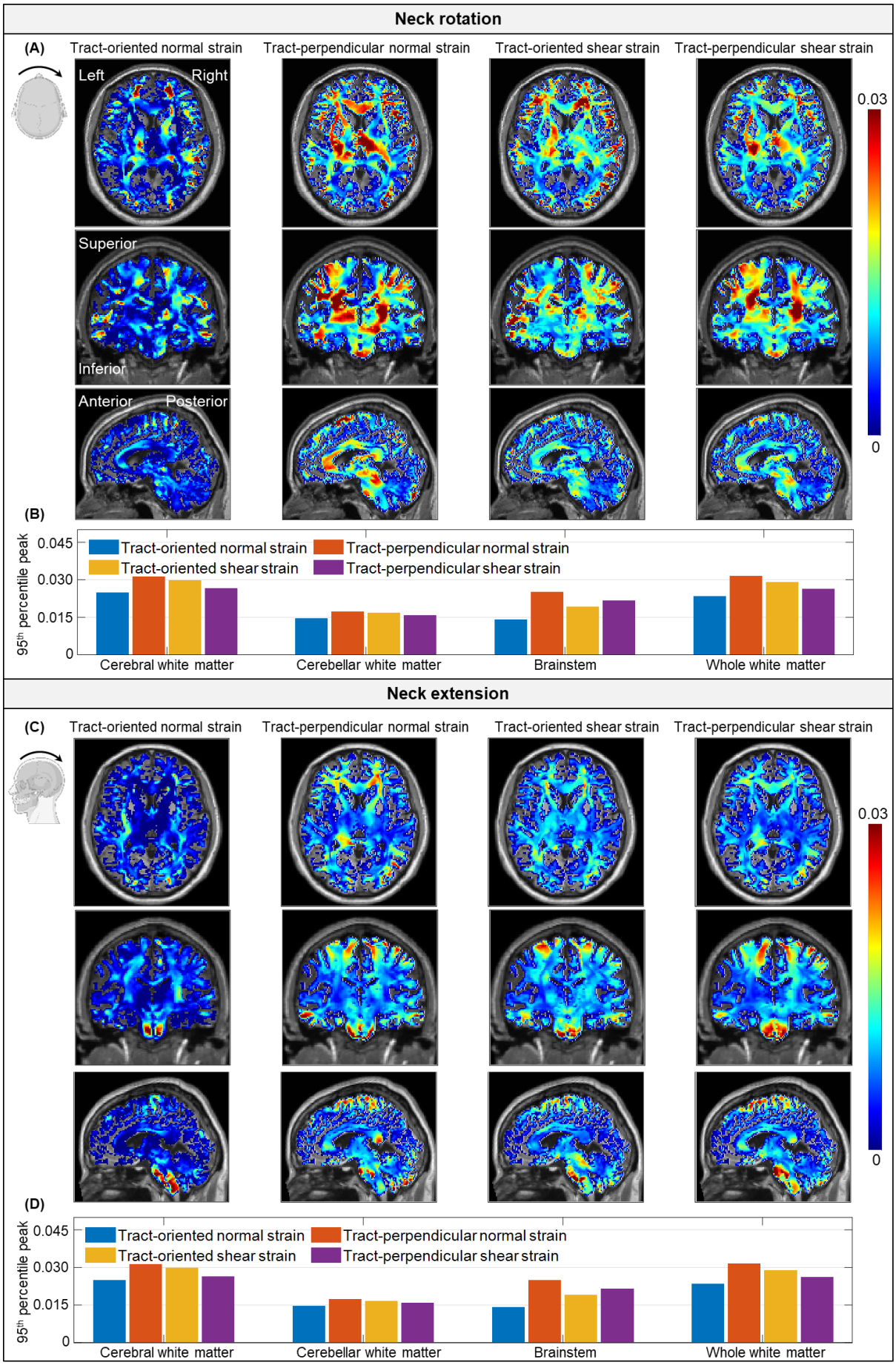
Neck rotation
(A)
Tract-oriented normal strain
Tract-perpendicular normal strain
Tract-oriented shear strain
Tract-perpendicular shear strain
Left
Right
Superior
Inferior
Anterior
Posterior
0.03
0
(B)
95th percentile peak
0.045
0.030
0.015
0
Tract-oriented normal strain
Tract-perpendicular normal strain
Tract-oriented shear strain
Tract-perpendicular shear strain
Cerebral white matter
Cerebellar white matter
Brainstem
Whole white matter
Neck extension
(C)
Tract-oriented normal strain
Tract-perpendicular normal strain
Tract-oriented shear strain
Tract-perpendicular shear strain
0.03
0
(D)
95th percentile peak
0.045
0.030
0.015
0
Tract-oriented normal strain
Tract-perpendicular normal strain
Tract-oriented shear strain
Tract-perpendicular shear strain
Cerebral white matter
Cerebellar white matter
Brainstem
Whole white matter

Fig 3. Time-accumulated tract-related strain peaks in one neck rotation (A-B) and one neck extension (C-D) that were conducted on the same subject. (A) Axial, coronal, and sagittal views of tract-oriented normal strain, tract-perpendicular normal strain, tract-oriented shear strain, tract-perpendicular shear strain (color), and T1-w MRI (grayscale) during neck rotation with 95th percentile peak values in three white matter subregions and the whole white matter shown in subfigure B. Similar plots are presented for neck extension in subfigures C-D. The anatomical orientation is specified in the tract-oriented normal strain contour during neck rotation in subfigure A.

At the group level, comparisons among four tract-related strain peaks are summarized in Fig 4. Across all regions of interest, the tract-perpendicular normal strain peaks are the largest and tract-oriented normal strains are the lowest (p < 0.001). Between the two tract-related shear strains, a significant difference (p = 0.002) is noted in the cerebral WM, although the difference is negligible (0.021 ± 0.007 for tract-oriented shear strain vs. 0.020 ± 0.007 for tract-perpendicular shear strain). No significant disparities (p > 0.05) are noted between these two shear strains in the cerebellar WM, brainstem, and whole WM. Detailed plots of inter-strain comparison are presented in Appendix C.

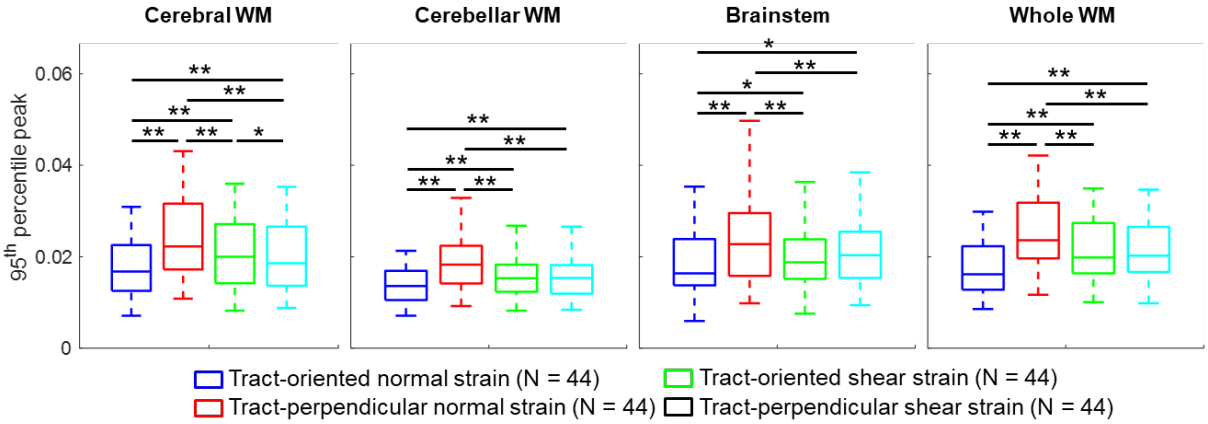

Fig 4. Comparisons of four tract-related strain peaks (95th percentile values) in cerebral white matter (WM), cerebellar WM, brainstem, and the whole WM (*p<0.05, **p<0.001, Wilcoxon matched-pairs signed-rank tests).

Comparison of tract-related strain peaks between neck rotations and neck extensions is analyzed in Fig 5. The average values for the peak change in angular velocity and peaking angular acceleration are 4.2 ± 1.2 rad/s (range: 1.8-6.4 rad/s) and 185.5 ± 59.2 rad/s^2 (range: 49.8-317.0 rad/s^2) for neck rotations (N = 30), and 2.1 ± 0.5 rad/s (range: 1.0~2.8 rad/s) and 228.6 ± 8.3 rad/s^2 (range: 63.8-345.6 rad/s^2) for neck extensions (N = 14). A significant difference (p<0.05) is noted for the peak change in angular velocity between two head loading modes (Fig 5A). A summary of tract-related strains in different WM areas is reported in Fig 5B. At the whole WM level, 95th percentile maximum tract-related strains (mean ± standard deviation (range)) in neck rotations are 0.020 ± 0.005 (0.009-0.030) for tract-oriented normal strain, 0.028 ± 0.007 (0.011-0.042) for tract-perpendicular normal strain, 0.024 ± 0.006 (0.010-0.035) for tract-oriented shear strain, and 0.023 ± 0.006 (0.010~0.035) for tract-perpendicular shear strain. For neck extensions, the maximum tract-oriented normal, tract-perpendicular normal, tract-oriented shear, and tract-perpendicular shear strains are 0.013 ± 0.002 (0.009-0.017), 0.019 ± 0.004 (0.012-0.024), 0.016 ± 0.003 (0.010-0.020), and 0.017 ± 0.003 (0.011-0.022), respectively. When comparing the strain peaks between neck rotations and neck extensions, significant differences (p<0.001) are noted in the cerebral WM and whole WM, independent of the strain type.

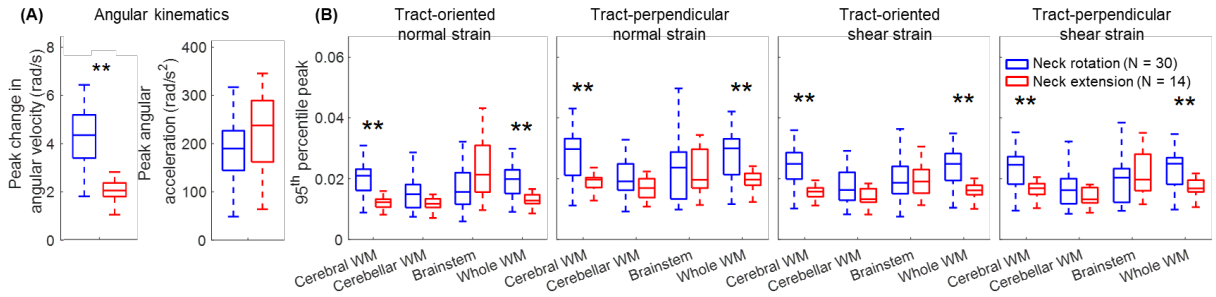

Fig 5. Influence of head loading mode on tract-related strains. (A) Comparisons of peak angular kinematics. (B) Comparison of four tract-related strain peaks (95th percentile values) in cerebral white matter (WM), cerebellar WM, brainstem, and the whole WM between neck rotation and neck extension (**p<0.001, Mann-Whitney U test).

Pearson's correction results between angular kinematics peaks (i.e., peak changes in angular velocity and peak angular acceleration) and maximum tract-related strain peaks (95th percentile values) are summarized in Table 1 with detailed plots in Appendix D. The correlation results are mainly dependent on the WM region and head loading mode. For the peak change in angular velocity, significant correlations are noted in cerebral WM and whole WM (all strain types) for neck rotation (Fig 5A), and in the brainstem (all strain types) and cerebellar WM (only tract-oriented shear strain) for neck extension (Fig 5B). When switching the kinematic parameters to peak angular acceleration, similar correlation results are noted, except that the Person's correlation coefficient values change slightly (Fig 5C-D).

Table 1. Person's correlation coefficients between peak angular kinematics (i.e., peak change in angular velocity, peak angular acceleration) and maximum tract-related strains (95th percentile peak) in cerebral white matter (WM), cerebellar WM, brainstem, and whole WM during neck rotation (A, C) and neck extension (B, D). For the significant correlation (p<0.05), the cells are coloured in dark yellow and the coefficients are in bold. For the insignificant correlation (p>0.05), the cells are coloured in light grey.

p <0.05 / p >0.05	Pearson's correlation coefficient values Tract-related strains vs. peak change in angular velocity								Pearson's correlation coefficient values Tract-related strains vs. peak angular acceleration							
	(A) Neck rotation (N=30)				(B) Neck extension (N=14)				(C) Neck rotation (N=30)				(D) Neck extension (N=14)			
	Cerebral WM	Cerebellar WM	Brainstem	Whole WM	Cerebral WM	Cerebellar WM	Brainstem	Whole WM	Cerebral WM	Cerebellar WM	Brainstem	Whole WM	Cerebral WM	Cerebellar WM	Brainstem	Whole WM
Tract-oriented normal strain	**0.46**	0.10	0.07	**0.43**	0.14	0.53	**0.67**	0.32	**0.46**	0.15	0.07	**0.43**	0.15	0.51	**0.65**	0.32
Tract-perpendicular normal strain	**0.52**	0.12	-0.02	**0.48**	0.20	0.46	**0.68**	0.31	**0.53**	0.14	0.01	**0.50**	0.19	0.46	**0.67**	0.31
Tract-oriented shear strain	**0.56**	0.17	0.02	**0.52**	0.16	**0.60**	**0.75**	0.32	**0.57**	0.18	0.01	**0.53**	0.15	**0.61**	**0.77**	0.31
Tract-perpendicular shear strain	**0.52**	0.12	0.06	**0.49**	0.24	0.48	**0.70**	0.34	**0.53**	0.12	0.08	**0.50**	0.24	0.45	**0.72**	0.33

Discussions

The current study estimates WM fiber deformation based on four tract-related strains under 42 volunteer impacts by relating the brain strain tensor measured by tMRI to fiber orientation estimated from DTI. This multimodal imaging analysis investigates four strain parameters (i.e., tract-oriented normal strain, tract-perpendicular normal strain, tract-oriented shear strain, and tract-perpendicular shear strain), collectively representing a comprehensive description of the fiber deformation. Our work finds the tract-perpendicular normal strain is the largest and tract-oriented normal strain is the lowest, unveiling fundamental new aspects of WM dynamics. The reported strain results can be used to evaluate the biofidelity of computational human head models, especially those intended to predict the brain strain

under non-injurious impacts.

Our work unravels the WM fiber tract deforms most in normal in the perpendicular direction, holding significant implications for brain injury mechanics. At present, the stretch along the fiber direction is widely recognized as the primary pathogenesis of axonal injury, as substantiated by the growing body of literature that employs tract-oriented normal strain as an axonal injury criterion [43, 53-57]. Indeed, several *in vitro* studies reported under the same magnitude level, the tract-oriented normal strain instigated severer axonal pathology than the tract-perpendicular normal strain [58, 59], indicating a higher tolerance level for the normal strain perpendicular to the neurites. However, our work finds that under *in vivo* human head impacts, the tract-perpendicular normal strain is significantly larger than the tract-oriented normal strain. Thereby, one cannot exclude the possibility that the tract-perpendicular strain is the major instigator of axonal pathology in real-world impacts. When switching to the shear strain, our work finds that the tract-oriented and tract-perpendicular shear strains are significantly larger than the tract-oriented normal strain. *In vitro* studies also observed neurite loss and neuron death in the regime when the tract-oriented shear strain peaked [60, 61]. Taken together, it can be concluded that the existing brain injury investigation may neglect important aspects of axonal pathogenesis.

The range of tract-related strains in our *in vivo* analyses are generally agreed with the regime in one early *in vivo* measurement of brain strain, and far smaller than the proposed brain injury thresholds from *in silico* studies and the strain magnitude in *in vitro* studies with axonal pathology (Table 2). In 2020, Knutsen, et al. [44] presented the first *in vivo* measurement of tract-oriented normal strain and reported the range to be 0.007-0.029, largely overlapping with the values in our study (0.009-0.030). *In silico* models have been used to develop brain injury thresholds based on the tract-oriented normal strain. For example, by relating binary injury outcomes (i.e., concussion or no concussion) in sports-related impacts with continuous tract-oriented normal strain data from computational simulations, Giordano and Kleiven [53] proposed an injury threshold of 0.09 for the corpus callosum and 0.15 for the brainstem. Hajiaghamemar and Margulies [27] co-registered the numerically derived tract-oriented normal strain contour with the histology-identified neuropathological map in piglets, reporting the axonal injury threshold fell within the range of 0.08-0.14. Similar thresholds were also developed for diffuse axonal injury in humans (0.15) [54], brain injury in nonhuman primates (0.12 for mild trauma and 0.19 for severe trauma) [55], and impact-induced behavioural changes in rats (0.09) [62]. A few *in vitro* studies linked the strain at the cultured tissue to the injury outcome. For example, LaPlaca and colleagues [61] found a significant loss of neurite that occurred at the conditions when the tract-oriented shear strain peaked (~0.56). In another *in vitro* model [60] with neuronal death, the tract-oriented normal and shear strains were within the range of 0.12-0.64 and 0.11-0.48, respectively. Bar-Kochba, et al. [63] found the axonal bleb formation was strongly correlated with the tract-oriented shear strain with a threshold of 0.14. Nakadate, et al. [59] found swelling in neurons aligned with and perpendicular to the loading

direction (a strain of 0.22 at a strain rate of 37 /s). Braun, et al. [58] also observed tau pathology in neurons oriented along and perpendicular to the loading direction at the strain magnitudes of 0.05 and 0.20 (strain rate: 10 /s), respectively. It should be clarified that the scale of interest may not necessarily be the same between the *in vitro* studies (axon/neuron level) and the current work (fiber tract level). Taken together, the tract-related strain values in *in silico* and *in vitro* studies with varying injury outcomes largely exceed the range in our study under *in vivo* volunteer impacts.

Table 2. Comparison of tract-related strains among *in vivo*, *in silico*, and *in vitro* studies. Note that the nomenclature in the listed studies may not be the same and are converted to the one in the current study. For the three superscripts, [a]: the values are estimated from Fig 7 of the cited reference; [b]: the values are estimated from Fig 4 of the cited reference; [c]: the values are estimated from Fig 9 of the cited reference; [d]: In the original article, the value was averaged along the length of neuron; [e]: the values are obtained based on the assumption that the strain levels in the embedded neuron are the same as those imposed to the cultured experimental tissue.

Reference		*Peak angular acceleration (rad/s²)*		*Tract-oriented normal strain*	*Tract-perpendicular normal strain*	*Tract-oriented shear strain*	*Tract-perpendicular shear strain*
In vivo	Current study	Neck rotation (N=30)	185.5 ± 59.2	0.009-0.030	0.011-0.042	0.010-0.035	0.010-0.035
		Neck extension (N=14)	228.6 ± 8.3	0.009-0.017	0.012-0.024	0.010-0.020	0.011-0.022
	Knutsen, et al. [44]	Neck rotation (N=10)	212.8 ± 32.1	0.007-0.024[a]			
		Neck extension (N=10)	282.8 ± 47.4	0.008-0.029[a]			
Reference		*Thresholds of 50% injury risk*		*Tract-oriented normal strain*	*Tract-perpendicular normal strain*	*Tract-oriented shear strain*	*Tract-perpendicular shear strain*
In silico	Giordano and Kleiven [53]	Concussion (human)		0.07-0.15			
	Sahoo, et al. [54]	Diffuse axonal injury (human)		0.15			
	Wu, et al. [55]	Brain injury (primate)		0.12-0.19			
	Hajiaghamemar and Margulies [27]	Diffuse axonal injury (pig)		0.08-0.14			
	Premi, et al. [62]	Behavioural alteration (rat)		0.09			
Reference		*Injury pathology*		*Tract-oriented normal strain*	*Tract-perpendicular normal strain*	*Tract-oriented shear strain*	*Tract-perpendicular shear strain*
In vitro	LaPlaca, et al. [61]	Neurite loss				~0.56[b]	
	Cullen and LaPlaca [60]	Neuron death		~0.12-0.64[c]		~0.11-0.48[c]	
	Bar-Kochba, et al. [63]	Neuron bleb formation				0.14[d]	
	Nakadate, et al. [59]	Neuron swelling		0.22[e]	0.22[e]		
	Braun, et al. [58]	Tau mislocalization		0.05[e]	0.2[e]		

Our results find interesting laterally symmetric patterns with respect to the midsagittal plane in all four tract-related strains under neck extensions, but not under neck extensions. This can be explained by the presence of cerebral falx at the interhemispheric fissure with mechanically stiffer properties than the brain (i.e., ~ 22.9 MPa for the elastic moduli of falx [64] vs. ~ 1 kPa level for the shear stiffness of the brain [65]). During neck extensions, the brain primarily moves within the sagittal plane (confirmed by the displacement field recorded by tMRI) with little interaction with the anterior-posterior oriented falx, and hence left-right symmetric deformation patterns are developed in the brain. Under neck rotations, the primary brain displacement is noted within the coronal plane. The presence of the mechanically stiffer falx disturbs the brain motion, leading to asymmetric strain patterns. Similar findings have been reported in earlier *in vivo* imaging studies [36, 44] and *in silico* impact simulations

[66, 67]. Collectively, these studies highlight the mechanical role of the falx during impacts.

Our study represents a significant extension of one early *in vivo* tract-oriented normal strain estimation (10 neck rotations and 10 neck extensions) [44] by involving more impacts (30 neck rotations and 14 neck extensions). Except for the overlap of the tract-oriented normal strain ranges described above, both our work and the early study [44] found high tract-oriented normal strains primarily in the cerebral WM for neck rotations and in the brainstem for neck extensions (Fig 3), providing independent verification of each other. Moreover, we generate spatially detailed information on how the axonal fiber responds to normal strain perpendicular to the fiber tract and shear strain along and perpendicular to the fiber tract, representing three new aspects of fiber deformation. Knutsen, et al. [44] found the square of angular velocity peak strongly correlated with the maximum tract-oriented normal strain in the corpus callosum during neck rotations and in the brainstem during neck extensions. Here, we expand the correlation by incorporating other kinematic-based metrics (i.e., peak change in angular velocity and peak angular acceleration) and four tract-related strains, through which we find both angular kinematics-based peaks significantly correlated with the tract-related strains (all four types) in cerebral WM and whole WM for neck rotations, and in the brainstem (all four types) and cerebellar WM (only the tract-oriented shear strain) for neck extensions (Table 1). To provide further verification of the observed relationships, in-house *in silico* work is ongoing to extend the correlation analyses by including impacts at high severity.

The current work provides important data for the validation of computational head models. Partially owing to the development of numerical algorithms such as the finite element method and material point method, computational head models have become increasingly used to study brain biomechanics [16]. Prior to the utilization, the reliability of computational head models requires to be extensively evaluated against relevant experimental measurements. Existing head models are often validated against cadaveric measurements in the form of brain-skull relative motion [7, 11, 68], maximum principal and shear strain [8, 9], and maximum principal strain rate [10] from only a handful of intracranial sites with the impact severities close to traumatic levels. Despite the great value of cadaveric tests, the material property of the brain changes after death. This is further complicated by the influence of post-mortem time and storage conditions without consensuses being reached yet [65]. One possible solution is to validate the model's responses collectively against the measurements from high-severity, sparsely recorded cadaveric experiments and low-severity, spatially detailed volunteer tests (such as the brain strain data presented herein). This may be particularly relevant for those models with intended usage to predict the brain response under non-injurious impacts. Emerging attempts have been noted in validating the computational head model against *in vivo* brain responses in the form of brain-skull relative displacement [69], maximum principal strain [21, 22, 67, 70], maximum shear strain [67], and tract-oriented normal strain [21, 22]. Our study computes 3D normal and shear strains along and perpendicular to the fiber tract (spatial resolution: 1 mm or 2 mm, temporal resolution: 18 ms, 19.5 ms,

or 20 ms) across the whole WM from 44 volunteer impacts. These strain data are complementary to the existing cadaveric experiments. Collectively, these *in vivo* and *in situ* experimental data may contribute to the validation of computational brain models towards a comprehensive degree and ensure the confidence of model usage to estimate brain response across the sub-injurious and injurious levels.

As motivated by the prevalence choice of using normal and shear strain (e.g., maximum principal strain, maximum shear strain) for brain injury analysis [71], the current study presents the normal strain and shear strain along and perpendicular to fiber tracts. Recent trends were noted in employing the compressive normal strain as the parameter of interest, e.g., minimum principal strain [72-74], compressive strain at the fiber tract level [75], neuronal level [63], and microtube level [76]. For example, two *in vitro* studies imposed compressive normal strains perpendicular to the main axonal direction and found cytoskeletal degeneration (e.g., changes in neurofilament and microtube distributions) [77, 78], suggesting the tract-perpendicular normal strain in compression as a possible trigger of axonal injury. In relation to our study, the tract-perpendicular normal strain at a given time instance may attain both positive value (i.e., tensile strain) and negative value (i.e., compressive strain) with dependency on the choice of coordinate systems (see equations 3-4 in Appendix A). Although the current study focuses on the tensile normal strain (e.g., $\varepsilon_t = \varepsilon_t^{\max}$ represents the maximum tract-perpendicular normal strain, see Appendix A), we also present the equation for computing the minimum tract-perpendicular strain across all tract-aligned coordinate systems (see $\varepsilon_t^{\min}$ in Appendix A). Other researchers, who are interested in computing the compressive normal strain perpendicular to the fiber tract, may find this equation helpful.

The current study is based on volunteer tests and imaging data from an open-access dataset. Despite its great value, the dataset suffers certain limitations that were already detailed by the dataset developer [42]. Other challenges and caveats, e.g., the limited number of image frames in tMRI [39, 44], the adverse effect of decreased signal-to-noise ratio on strain estimation as tag lines fade [79], incapability of diffusion tensor to describe the region of crossing fibers with multiple orientations present within the voxel [80, 81], are exhaustively discussed elsewhere and not reiterated herein.

Conclusion

This study calculates WM tract-related deformation during voluntary impacts by relating the tMRI-recorded brain strain tensor to DTI-derived fiber orientation through coordinate transformation. By extending the previous effort that focused on the normal strain along the fiber tract, we present *in vivo* data of the normal strain perpendicular to the fiber tract and shear strain along and perpendicular to the fiber tract towards a multifaceted understanding of WM dynamics. Our work finds the fiber tract deforms most in the perpendicular direction, deciphering new fundamentals of brain biomechanics. The reported strain results under volunteer impacts can be used to evaluate the fidelity of computational head models, especially those intended to predict brain strains under non-injurious conditions.

Availability of data and materials

All strain data computed herein, including 4 tract-related strains from 44 impacts, can be requested by emailing request to the corresponding author and are planned to be open-accessed via the original dataset.

Funding

This research has received funding from KTH Royal Institute of Technology (Stockholm, Sweden) and the Swedish Governmental Agency for Innovation systems (VINNOVA) (no. 2023-00753).

Acknowledgement

Data were provided in part by the Brain Biomechanics Imaging Repository (http://www.nitrc.org/projects/bbir). Principal Investigators: P. Bayly, D. Pham, C. Johnson, J. Prince, K. Ramesh, through grants U01 NS11212 and R56 NS055951. The content of this article is solely the responsibility of the authors and does not necessarily represent the official views of neither funding agencies nor the dataset developer. The computation of tract-related strains was enabled by resources provided by the National Academic Infrastructure for Supercomputing in Sweden (NAISS) at the center for High Performance Computing (PDC) partially funded by the Swedish Research Council through grant agreement no. 2022-06725.

Conflict of Interest

The authors declare that they have no conflict of interest.

Author contribution

Zhou Zhou: Conceptualization, Formal analysis, Funding acquisition, Methodology, Software, Visualization, Original draft, Review & editing. **Christoffer Olsson**: Conception and study design, Investigation, Software, Review & editing. **T. Christian Gasser**: Formal analysis, Investigation, Methodology, Original draft, Review & editing. **Xiaogai Li**: Visualization, Methodology, Review & editing. **Svein Kleiven**: Methodology, Original draft, Review & editing, Funding acquisition.

References

[1] M.C. Dewan, A. Rattani, S. Gupta, R.E. Baticulon, Y.-C. Hung, M. Punchak, A. Agrawal, A.O. Adeleye, M.G. Shrime, A.M. Rubiano, Estimating the global incidence of traumatic brain injury, Journal of neurosurgery, 130 (2018) 1080-1097.
[2] A. Brazinova, V. Rehorcikova, M.S. Taylor, V. Buckova, M. Majdan, M. Psota, W. Peeters, V. Feigin, A. Theadom, L. Holkovic, Epidemiology of traumatic brain injury in Europe: a living systematic review, Journal of neurotrauma, 38 (2021) 1411-1440.
[3] K. Pedersen, M. Fahlstedt, A. Jacobsson, S. Kleiven, H. Von Holst, A national survey of traumatic brain injuries admitted to hospitals in Sweden from 1987 to 2010, Neuroepidemiology, 45 (2015) 20-27.

[4] A.I. Maas, D.K. Menon, G.T. Manley, M. Abrams, C. Åkerlund, N. Andelic, M. Aries, T. Bashford, M.J. Bell, Y.G. Bodien, Traumatic brain injury: progress and challenges in prevention, clinical care, and research, The Lancet Neurology, 21 (2022) 1004-1060.
[5] A. Alshareef, J. Giudice, D. Shedd, K. Reynier, T. Wu, M. Panzer, Experimental data for validating the structural response of computational brain models, Multiscale Biomechanical Modeling of the Brain, Elsevier2022, pp. 193-208.
[6] W.N. Hardy, Response of the human cadaver head to impact, Wayne State University, 2007.
[7] W.N. Hardy, M.J. Mason, C.D. Foster, C.S. Shah, J.M. Kopacz, K.H. Yang, A.I. King, J. Bishop, M. Bey, W. Anderst, A study of the response of the human cadaver head to impact, Stapp car crash journal, 51 (2007) 17-80.
[8] Z. Zhou, X. Li, S. Kleiven, W.N. Hardy, Brain Strain from Motion of Sparse Markers, Stapp car crash journal, 63 (2019) 1-27.
[9] Z. Zhou, X. Li, S. Kleiven, C. Shah, W. Hardy, A Reanalysis of Experimental Brain Strain Data: Implication for Finite Element Head Model Validation, Stapp car Crash Journal, 62 (2018) 293-318.
[10] Z. Zhou, X. Li, Y. Liu, W.N. Hardy, S. Kleiven, Brain strain rate response: addressing computational ambiguity and experimental data for model validation, Brain Multiphysics, 4 (2023) 100073.
[11] A. Alshareef, J.S. Giudice, J. Forman, D.F. Shedd, K.A. Reynier, T. Wu, S. Sochor, M.R. Sochor, R.S. Salzar, M.B. Panzer, Biomechanics of the human brain during dynamic rotation of the head, Journal of neurotrauma, 37 (2020) 1546-1555.
[12] B. Morrison III, B.S. Elkin, J.-P. Dollé, M.L. Yarmush, In vitro models of traumatic brain injury, Annual review of biomedical engineering, 13 (2011) 91-126.
[13] Y.-H. Wu, S. Rosset, T.-r. Lee, M. Dragunow, T. Park, V. Shim, In vitro models of traumatic brain injury: A systematic review, Journal of Neurotrauma, 38 (2021) 2336-2372.
[14] H.L. Cater, L.E. Sundstrom, B. Morrison III, Temporal development of hippocampal cell death is dependent on tissue strain but not strain rate, Journal of biomechanics, 39 (2006) 2810-2818.
[15] W.H. Kang, B. Morrison III, Functional tolerance to mechanical deformation developed from organotypic hippocampal slice cultures, Biomechanics and modeling in mechanobiology, 14 (2015) 561-575.
[16] S. Ji, M. Ghajari, H. Mao, R.H. Kraft, M. Hajiaghamemar, M.B. Panzer, R. Willinger, M.D. Gilchrist, S. Kleiven, J.D. Stitzel, Use of brain biomechanical models for monitoring impact exposure in contact sports, Annals of Biomedical Engineering, 50 (2022) 1389-1408.
[17] A. Madhukar, M. Ostoja-Starzewski, Finite element methods in human head impact simulations: a review, Annals of biomedical engineering, 47 (2019) 1832-1854.
[18] J.S. Giudice, A. Alshareef, T. Wu, C.A. Gancayco, K.A. Reynier, N.J. Tustison, T.J. Druzgal, M.B. Panzer, An image registration-based morphing technique for generating subject-specific brain finite element models, Annals of Biomedical Engineering, 48 (2020) 2412-2424.
[19] X. Li, Subject-specific head model generation by mesh morphing: a personalization framework and its applications, Frontiers in bioengineering and biotechnology, 9 (2021) 706566.
[20] C. Giordano, R. Cloots, J. Van Dommelen, S. Kleiven, The influence of anisotropy on brain injury prediction, Journal of biomechanics, 47 (2014) 1052-1059.
[21] A. Alshareef, A.K. Knutsen, C.L. Johnson, A. Carass, K. Upadhyay, P.V. Bayly, D.L. Pham, J.L. Prince, K. Ramesh, Integrating material properties from magnetic resonance elastography into subject-specific computational models for the human brain, Brain multiphysics, 2 (2021) 100038.
[22] K. Upadhyay, A. Alshareef, A.K. Knutsen, C.L. Johnson, A. Carass, P.V. Bayly, D.L. Pham, J.L. Prince, K. Ramesh, Development and validation of subject-specific 3D human head models based on a nonlinear visco-hyperelastic constitutive framework, Journal of the Royal Society Interface, 19 (2022) 20220561.
[23] Z. Zhou, X. Li, S. Kleiven, Fluid–structure interaction simulation of the brain–skull interface for acute subdural haematoma prediction, Biomechanics and modeling in mechanobiology, 18 (2019) 155-173.
[24] Z. Zhou, X. Li, S. Kleiven, Evaluation of brain-skull interface modelling approaches on the prediction of acute subdural hematoma in the elderly, Journal of biomechanics, 105 (2020) 109787.

[25] A. Montanino, X. Li, Z. Zhou, M. Zeineh, D. Camarillo, S. Kleiven, Subject-specific multiscale analysis of concussion: from macroscopic loads to molecular-level damage, Brain multiphysics, 2 (2021) 100027.
[26] Q. Yuan, X. Li, Z. Zhou, S. Kleiven, A novel framework for video-informed reconstructions of sports accidents: A case study correlating brain injury pattern from multimodal neuroimaging with finite element analysis, Brain Multiphysics, 6 (2024) 100085.
[27] M. Hajiaghamemar, S.S. Margulies, Multi-scale white matter tract embedded brain finite element model predicts the location of traumatic diffuse axonal injury, Journal of Neurotrauma, 38 (2021) 144-157.
[28] C. Zhang, L. Bartels, A. Clansey, J. Kloiber, D. Bondi, P. van Donkelaar, L. Wu, A. Rauscher, S. Ji, A computational pipeline towards large-scale and multiscale modeling of traumatic axonal injury, Computers in Biology and Medicine, (2024) 108109.
[29] P.V. Bayly, E.H. Clayton, G.M. Genin, Quantitative imaging methods for the development and validation of brain biomechanics models, Annual review of biomedical engineering, 14 (2012) 369-396.
[30] P.J. McCracken, A. Manduca, J. Felmlee, R.L. Ehman, Mechanical transient-based magnetic resonance elastography, Magnetic Resonance in Medicine, 53 (2005) 628-639.
[31] R. Muthupillai, D. Lomas, P. Rossman, J.F. Greenleaf, A. Manduca, R.L. Ehman, Magnetic resonance elastography by direct visualization of propagating acoustic strain waves, science, 269 (1995) 1854-1857.
[32] J. Abderezaei, A. Pionteck, I. Terem, L. Dang, M. Scadeng, P. Morgenstern, R. Shrivastava, S.J. Holdsworth, Y. Yang, M. Kurt, Development, calibration, and testing of 3D amplified MRI (aMRI) for the quantification of intrinsic brain motion, Brain Multiphysics, 2 (2021) 100022.
[33] T.G. Reese, D.A. Feinberg, J. Dou, V.J. Wedeen, Phase contrast MRI of myocardial 3D strain by encoding contiguous slices in a single shot, Magnetic Resonance in Medicine: An Official Journal of the International Society for Magnetic Resonance in Medicine, 47 (2002) 665-676.
[34] E.A. Zerhouni, D.M. Parish, W.J. Rogers, A. Yang, E.P. Shapiro, Human heart: tagging with MR imaging--a method for noninvasive assessment of myocardial motion, Radiology, 169 (1988) 59-63.
[35] P.V. Bayly, T. Cohen, E. Leister, D. Ajo, E. Leuthardt, G. Genin, Deformation of the human brain induced by mild acceleration, Journal of neurotrauma, 22 (2005) 845-856.
[36] A.A. Sabet, E. Christoforou, B. Zatlin, G.M. Genin, P.V. Bayly, Deformation of the human brain induced by mild angular head acceleration, Journal of biomechanics, 41 (2008) 307-315.
[37] Y. Feng, T.M. Abney, R.J. Okamoto, R.B. Pless, G.M. Genin, P.V. Bayly, Relative brain displacement and deformation during constrained mild frontal head impact, Journal of the Royal Society Interface, 7 (2010) 1677-1688.
[38] A.K. Knutsen, E. Magrath, J.E. McEntee, F. Xing, J.L. Prince, P.V. Bayly, J.A. Butman, D.L. Pham, Improved measurement of brain deformation during mild head acceleration using a novel tagged MRI sequence, Journal of biomechanics, 47 (2014) 3475-3481.
[39] A.D. Gomez, A.K. Knutsen, F. Xing, Y.-C. Lu, D. Chan, D.L. Pham, P. Bayly, J.L. Prince, 3-D measurements of acceleration-induced brain deformation via harmonic phase analysis and finite-element models, IEEE Transactions on Biomedical Engineering, 66 (2018) 1456-1467.
[40] F. Xing, J. Woo, A.D. Gomez, D.L. Pham, P.V. Bayly, M. Stone, J.L. Prince, Phase vector incompressible registration algorithm for motion estimation from tagged magnetic resonance images, IEEE transactions on medical imaging, 36 (2017) 2116-2128.
[41] D.D. Chan, A.K. Knutsen, Y.-C. Lu, S.H. Yang, E. Magrath, W.-T. Wang, P.V. Bayly, J.A. Butman, D.L. Pham, Statistical characterization of human brain deformation during mild angular acceleration measured in vivo by tagged magnetic resonance imaging, Journal of biomechanical engineering, 140 (2018) 101005.
[42] P.V. Bayly, A. Alshareef, A.K. Knutsen, K. Upadhyay, R.J. Okamoto, A. Carass, J.A. Butman, D.L. Pham, J.L. Prince, K. Ramesh, MR imaging of human brain mechanics in vivo: new measurements to facilitate the development of computational models of brain injury, Annals of biomedical engineering, 49 (2021) 2677-2692.
[43] R.M. Wright, A. Post, B. Hoshizaki, K.T. Ramesh, A multiscale computational approach to estimating axonal damage under inertial loading of the head, Journal of neurotrauma, 30 (2013) 102-118.

[44] A.K. Knutsen, A.D. Gomez, M. Gangolli, W.-T. Wang, D. Chan, Y.-C. Lu, E. Christoforou, J.L. Prince, P.V. Bayly, J.A. Butman, In vivo estimates of axonal stretch and 3D brain deformation during mild head impact, Brain multiphysics, 1 (2020) 100015.
[45] S. Ji, W. Zhao, J.C. Ford, J.G. Beckwith, R.P. Bolander, R.M. Greenwald, L.A. Flashman, K.D. Paulsen, T.W. McAllister, Group-wise evaluation and comparison of white matter fiber strain and maximum principal strain in sports-related concussion, Journal of neurotrauma, 32 (2015) 441-454.
[46] S. Sullivan, S.A. Eucker, D. Gabrieli, C. Bradfield, B. Coats, M.R. Maltese, J. Lee, C. Smith, S.S. Margulies, White matter tract-oriented deformation predicts traumatic axonal brain injury and reveals rotational direction-specific vulnerabilities, Biomechanics and modeling in mechanobiology, 14 (2015) 877-896.
[47] R.W. Carlsen, A.L. Fawzi, Y. Wan, H. Kesari, C. Franck, A quantitative relationship between rotational head kinematics and brain tissue strain from a 2-D parametric finite element analysis, Brain Multiphysics, 2 (2021) 100024.
[48] M. Jenkinson, P. Bannister, M. Brady, S. Smith, Improved optimization for the robust and accurate linear registration and motion correction of brain images, Neuroimage, 17 (2002) 825-841.
[49] M. Jenkinson, S. Smith, A global optimisation method for robust affine registration of brain images, Medical image analysis, 5 (2001) 143-156.
[50] X. Zhan, Y. Li, Y. Liu, A.G. Domel, H.V. Alizadeh, Z. Zhou, N.J. Cecchi, S.J. Raymond, S. Tiernan, J. Ruan, Predictive factors of kinematics in traumatic brain injury from head impacts based on statistical interpretation, Annals of biomedical engineering, 49 (2021) 2901-2913.
[51] C.M. Huber, D.A. Patton, J. Maheshwari, Z. Zhou, S. Kleiven, K.B. Arbogast, Finite element brain deformation in adolescent soccer heading, Computer methods in biomechanics and biomedical engineering, (2023) 1-11.
[52] Z. Zhou, X. Li, A.G. Domel, E.L. Dennis, M. Georgiadis, Y. Liu, S.J. Raymond, G. Grant, S. Kleiven, D. Camarillo, The presence of the temporal horn exacerbates the vulnerability of hippocampus during head impacts, Frontiers in Bioengineering and Biotechnology, 10 (2022) 754344.
[53] C. Giordano, S. Kleiven, Evaluation of Axonal Strain as a Predictor for Mild Traumatic Brain Injuries Using Finite Element Modeling, Stapp car Crash Journal, 58 (2014) 29-61.
[54] D. Sahoo, C. Deck, R. Willinger, Brain injury tolerance limit based on computation of axonal strain, Accident Analysis & Prevention, 92 (2016) 53-70.
[55] T. Wu, M. Hajiaghamemar, J.S. Giudice, A. Alshareef, S.S. Margulies, M.B. Panzer, Evaluation of tissue-level brain injury metrics using species-specific simulations, Journal of neurotrauma, 38 (2021) 1879-1888.
[56] W. Zhao, Y. Cai, Z. Li, S. Ji, Injury prediction and vulnerability assessment using strain and susceptibility measures of the deep white matter, Biomechanics and modeling in mechanobiology, 16 (2017) 1709-1727.
[57] T. Wu, J. Antona-Makoshi, A. Alshareef, J.S. Giudice, M.B. Panzer, Investigation of cross-species scaling methods for traumatic brain injury using finite element analysis, Journal of neurotrauma, 37 (2020) 410-422.
[58] N.J. Braun, D. Liao, P.W. Alford, Orientation of neurites influences severity of mechanically induced tau pathology, Biophysical journal, 120 (2021) 3272-3282.
[59] H. Nakadate, E. Kurtoglu, H. Furukawa, S. Oikawa, S. Aomura, A. Kakuta, Y. Matsui, Strain-Rate Dependency of Axonal Tolerance for Uniaxial Stretching, Stapp car Crash Journal, 61 (2017) 53-65.
[60] D.K. Cullen, M.C. LaPlaca, Neuronal response to high rate shear deformation depends on heterogeneity of the local strain field, Journal of neurotrauma, 23 (2006) 1304-1319.
[61] M.C. LaPlaca, D.K. Cullen, J.J. McLoughlin, R.S. Cargill II, High rate shear strain of three-dimensional neural cell cultures: a new in vitro traumatic brain injury model, Journal of biomechanics, 38 (2005) 1093-1105.
[62] S. Premi, C. Deck, B.D. Stemper, R. Willinger, Mechanical threshold for concussion based on computation of axonal strain using a finite element rat brain model, Brain Multiphysics, 2 (2021) 100032.
[63] E. Bar-Kochba, M.T. Scimone, J.B. Estrada, C. Franck, Strain and rate-dependent neuronal injury in a 3D in vitro compression model of traumatic brain injury, Scientific reports, 6 (2016) 30550.

[64] D.R. Walsh, A.M. Ross, D.T. Newport, Z. Zhou, J. Kearns, C. Fearon, J. Lorigan, J.J. Mulvihill, Mechanical characterisation of the human dura mater, falx cerebri and superior sagittal sinus, Acta Biomaterialia, 134 (2021) 388-400.
[65] S. Budday, T.C. Ovaert, G.A. Holzapfel, P. Steinmann, E. Kuhl, Fifty shades of brain: a review on the mechanical testing and modeling of brain tissue, Archives of Computational Methods in Engineering, 27 (2020) 1187-1230.
[66] J. Ho, Z. Zhou, X. Li, S. Kleiven, The peculiar properties of the falx and tentorium in brain injury biomechanics, Journal of biomechanics, 60 (2017) 243-247.
[67] Y.-C. Lu, N.P. Daphalapurkar, A. Knutsen, J. Glaister, D. Pham, J. Butman, J. Prince, P. Bayly, K. Ramesh, A 3D computational head model under dynamic head rotation and head extension validated using live human brain data, including the falx and the tentorium, Annals of biomedical engineering, 47 (2019) 1923-1940.
[68] W. Hardy, C. Foster, M. Mason, K. Yang, A. King, S. Tashman, Investigation of Head Injury Mechanisms Using Neutral Density Technology and High-Speed Biplanar X-ray, Stapp car Crash Journal, 45 (2001) 337-368.
[69] F. Hernandez, C. Giordano, M. Goubran, S. Parivash, G. Grant, M. Zeineh, D. Camarillo, Lateral impacts correlate with falx cerebri displacement and corpus callosum trauma in sports-related concussions, Biomechanics and modeling in mechanobiology, 18 (2019) 631-649.
[70] W. Zhao, S. Ji, Displacement-and strain-based discrimination of head injury models across a wide range of blunt conditions, Annals of biomedical engineering, 48 (2020) 1661-1677.
[71] B. Rowson, S.M. Duma, A review of head injury metrics used in automotive safety and sports protective equipment, Journal of biomechanical engineering, 144 (2022) 110801.
[72] L.E. Miller, J.E. Urban, E.M. Davenport, A.K. Powers, C.T. Whitlow, J.A. Maldjian, J.D. Stitzel, Brain strain: computational model-based metrics for head impact exposure and injury correlation, Annals of biomedical engineering, 49 (2021) 1083-1096.
[73] S. Ji, S. Wu, W. Zhao, Dynamic characteristics of impact-induced brain strain in the corpus callosum, Brain Multiphysics, 3 (2022) 100046.
[74] C. Bradfield, L. Voo, D. Drewry III, V. Koliatsos, K. Ramesh, Dynamic strain fields of the mouse brain during rotation, Biomechanics and Modeling in Mechanobiology, (2023) 1-16.
[75] H.T. Garimella, R.H. Kraft, Modeling the mechanics of axonal fiber tracts using the embedded finite element method, International journal for numerical methods in biomedical engineering, 33 (2017) e2823.
[76] M. Soheilypour, M. Peyro, S.J. Peter, M.R. Mofrad, Buckling behavior of individual and bundled microtubules, Biophysical journal, 108 (2015) 1718-1726.
[77] A.J. Fournier, J.D. Hogan, L. Rajbhandari, S. Shrestha, A. Venkatesan, K. Ramesh, Changes in neurofilament and microtubule distribution following focal axon compression, PloS one, 10 (2015) e0131617.
[78] A.J. Fournier, L. Rajbhandari, S. Shrestha, A. Venkatesan, K. Ramesh, In vitro and in situ visualization of cytoskeletal deformation under load: traumatic axonal injury, The FASEB Journal, 28 (2014) 5277-5287.
[79] Z. Bian, A. Alshareef, S. Wei, J. Chen, Y. Wang, J. Woo, D.L. Pham, J. Zhuo, A. Carass, J.L. Prince, Is Registering Raw Tagged-MR Enough for Strain Estimation in the Era of Deep Learning?, arXiv preprint arXiv:2401.17571, (2024).
[80] B. Jeurissen, A. Leemans, J.D. Tournier, D.K. Jones, J. Sijbers, Investigating the prevalence of complex fiber configurations in white matter tissue with diffusion magnetic resonance imaging, Human brain mapping, 34 (2013) 2747-2766.
[81] Z. Zhou, T. Wang, D. Jörgens, X. Li, Fiber orientation downsampling compromises the computation of white matter tract-related deformation, journal of the mechanical behavior of biomedical materials, 132 (2022) 105294.
[82] M.T. Scimone, H.C. Cramer III, E. Bar-Kochba, R. Amezcua, J.B. Estrada, C. Franck, Modular approach for resolving and mapping complex neural and other cellular structures and their associated deformation fields in three dimensions, Nature protocols, 13 (2018) 3042-3064.
[83] Z. Zhou, X. Li, Y. Liu, M. Fahlstedt, M. Georgiadis, X. Zhan, S.J. Raymond, G. Grant, S. Kleiven, D. Camarillo, Toward a comprehensive delineation of white matter tract-related deformation, Journal of neurotrauma, 38 (2021) 3260-3278.

Appendix A Computation of tract-related strains

At a given time instance, the white matter (WM) tract-related strains are calculated by transforming the brain strain tensor to the coordinate system with one axis aligned with the fiber orientation. For a WM voxel (i.e., voxel with the fractional anisotropy value ≥0.2), the primary fiber orientation is approximated as the first principal eigenvector of diffusion tensor (denoted as $\boldsymbol{v} = [v_1 \quad v_2 \quad v_3]^{\mathrm{T}}$). At each time frame, the brain strain tensor $\boldsymbol{E}_{\mathrm{global}}$ in tagged magnetic resonance imaging (tMRI) (Fig 1C) is expressed with reference to the global coordinate system ($\boldsymbol{XYZ}$, $\boldsymbol{X} = [1 \quad 0 \quad 0]^{\mathrm{T}}$, $\boldsymbol{Y} = [0 \quad 1 \quad 0]^{\mathrm{T}}$, $\boldsymbol{Z} = [0 \quad 0 \quad 1]^{\mathrm{T}}$).

As shown in Fig A1A, we rotate $\boldsymbol{E}_{\mathrm{global}}$ into the local coordinate system (1) ($\boldsymbol{xyz}$, $\boldsymbol{x}$ is aligned with $\boldsymbol{v}$, $\boldsymbol{y}$ is the cross product of $\boldsymbol{x}$ and $\boldsymbol{X}$, $\boldsymbol{z}$ is the cross product of $\boldsymbol{x}$ and $\boldsymbol{y}$) via $\boldsymbol{E}_{\mathrm{tract}} = \boldsymbol{Q}\boldsymbol{E}_{\mathrm{global}}\boldsymbol{Q}^{\mathrm{T}}$, in which

$$\boldsymbol{Q} = \begin{bmatrix} \cos(\boldsymbol{x},\boldsymbol{X}) & \cos(\boldsymbol{x},\boldsymbol{Y}) & \cos(\boldsymbol{x},\boldsymbol{Z}) \\ \cos(\boldsymbol{y},\boldsymbol{X}) & \cos(\boldsymbol{y},\boldsymbol{Y}) & \cos(\boldsymbol{y},\boldsymbol{Z}) \\ \cos(\boldsymbol{z},\boldsymbol{X}) & \cos(\boldsymbol{z},\boldsymbol{Y}) & \cos(\boldsymbol{z},\boldsymbol{Z}) \end{bmatrix} = \begin{bmatrix} v_1 & v_2 & v_3 \\ 0 & \dfrac{-v_3}{\sqrt{(v_2^2+v_3^2)}} & \dfrac{v_2}{\sqrt{(v_2^2+v_3^2)}} \\ \sqrt{(v_2^2+v_3^2)} & \dfrac{-v_1 v_2}{\sqrt{(v_2^2+v_3^2)}} & \dfrac{-v_1 v_3}{\sqrt{(v_2^2+v_3^2)}} \end{bmatrix} \tag{1}$$

The six independent strain components in the local coordinate system (1) are illustrated in Fig A1C.

With respect to strain components ε_{xx}, γ_{xy}, and γ_{xz} (the latter two act at the plane perpendicular to the fiber direction, i.e., yz plane, see Fig A1D), we form two strain measures, i.e., the tract-oriented normal strain $\varepsilon_a = \varepsilon_{xx}$ represents the normal strain along the fiber tract (Fig A1E), and the shear strain $\gamma_a = \sqrt{\gamma_{xy}^2 + \gamma_{xz}^2}$ within the yz plane. Given the symmetry of the strain tensor, γ_a also appears along the fiber and it therefore denotes the tract-oriented shear strain (Fig A1E).

Now we consider the strain components ε_{yy}, ε_{zz}, γ_{yz} acting on the xy and xz planes (Fig A1C). Rotating these planes around the fiber direction changes the values of the individual strain components (i.e., $\boldsymbol{E}_{\mathrm{tract}(i)} = \boldsymbol{Q}_{\theta_i}\boldsymbol{E}_{\mathrm{tract}}\boldsymbol{Q}_{\theta_i}^{\mathrm{T}}$ in the local coordinate system (i) ($\boldsymbol{xy}_i\boldsymbol{z}_i$)) with dependency on the rotating angle ($0° < \theta_i < 360°$) (see Fig A1B). Note that

$$\boldsymbol{Q}_{\theta_i} = \begin{bmatrix} \cos(\boldsymbol{x},\boldsymbol{x}) & \cos(\boldsymbol{x},\boldsymbol{y}) & \cos(\boldsymbol{x},\boldsymbol{z}) \\ \cos(\boldsymbol{y}_i,\boldsymbol{x}) & \cos(\boldsymbol{y}_i,\boldsymbol{y}) & \cos(\boldsymbol{y}_i,\boldsymbol{z}) \\ \cos(\boldsymbol{z}_i,\boldsymbol{x}) & \cos(\boldsymbol{z}_i,\boldsymbol{y}) & \cos(\boldsymbol{z}_i,\boldsymbol{z}) \end{bmatrix} = \begin{bmatrix} 1 & 0 & 0 \\ 0 & \cos\theta_i & -\sin\theta_i \\ 0 & \sin\theta_i & \cos\theta_i \end{bmatrix} \tag{2}$$

The equations for the strain components ε_{yy}, ε_{zz}, γ_{yz} in $\boldsymbol{E}_{\mathrm{tract}(i)}$ are

$$\varepsilon_{y_iy_i}(\theta_i) = \frac{\varepsilon_{yy}+\varepsilon_{zz}}{2} - \sqrt{(\frac{\varepsilon_{yy}-\varepsilon_{zz}}{2})^2+\gamma_{yz}^2}\,\sin(2\theta_i+\varphi_1)\ (\varphi_1 = \arctan(\frac{\varepsilon_{yy}-\varepsilon_{zz}}{2\gamma_{yz}})) \tag{3}$$

$$\varepsilon_{z_iz_i}(\theta_i) = \frac{\varepsilon_{yy}+\varepsilon_{zz}}{2} + \sqrt{(\frac{\varepsilon_{yy}-\varepsilon_{zz}}{2})^2+\gamma_{yz}^2}\,\sin(2\theta_i+\varphi_2)\ (\varphi_2 = \arctan(\frac{\varepsilon_{zz}-\varepsilon_{yy}}{2\gamma_{yz}})) \tag{4}$$

$$\varepsilon_{y_iz_i}(\theta_i) = \sqrt{(\frac{\varepsilon_{yy}-\varepsilon_{zz}}{2})^2+\gamma_{yz}^2}\,\sin(2\theta_i+\varphi_3)\ (\varphi_3 = \arctan(\frac{2\gamma_{yz}}{\varepsilon_{yy}-\varepsilon_{zz}})) \tag{5}$$

Based on equations 3-4, $\varepsilon_t^{\max} = \bar{\bar{\varepsilon}} + \gamma_t$ denotes the maximum tract-perpendicular normal strain, and $\varepsilon_t^{\min} = \bar{\bar{\varepsilon}} - \gamma_t$ represents the minimum tract-perpendicular normal strain, where $\bar{\bar{\varepsilon}} = (\varepsilon_{yy} + \varepsilon_{zz})/2$. Based on equation 5, we determine the maximum tract-perpendicular shear strain $\gamma_t = \sqrt{\bar{\varepsilon}^2 + \gamma_{yz}^2}$, where $\bar{\varepsilon} = (\varepsilon_{yy} - \varepsilon_{zz})/2$.

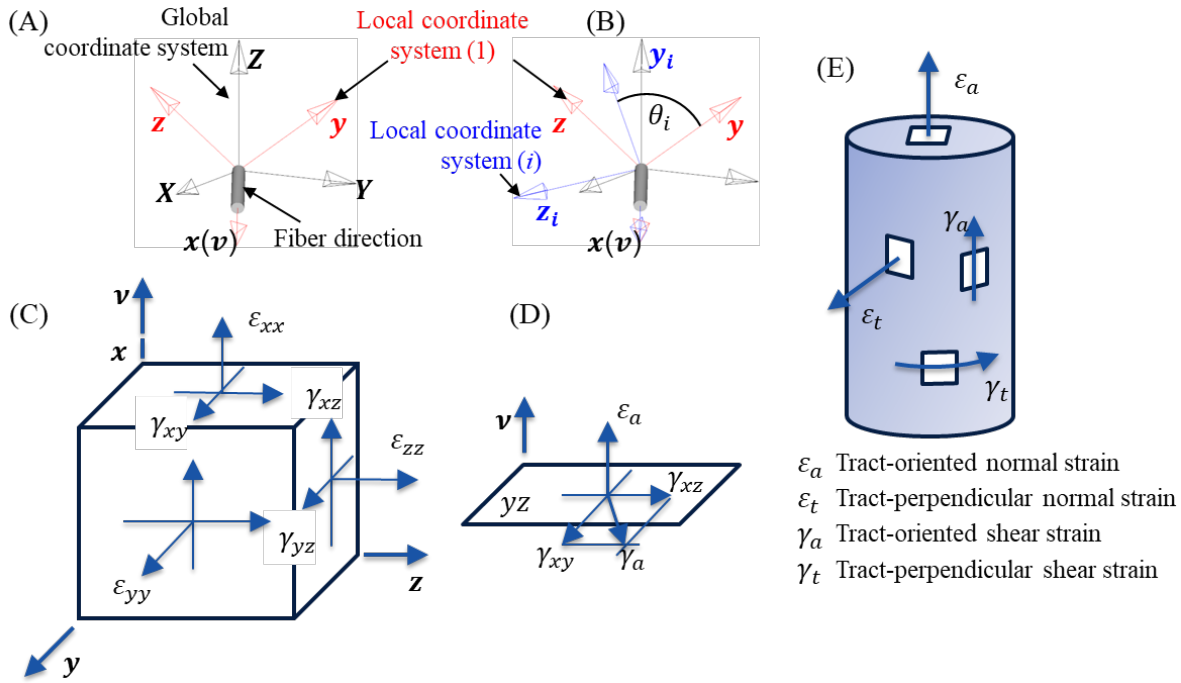

Fig A1. Computation of four tract-related strains via coordinate transformation. (A) Rotate the strain tensor from the global coordinate system ($\boldsymbol{XYZ}$) to the local coordinate system (1) ($\boldsymbol{xyz}$), in which $\boldsymbol{x}$ represents the fiber direction ($\boldsymbol{v}$). (B) Rotate the strain tensor from the local coordinate system (1) to the local coordinate system (i) ($\boldsymbol{xy_iz_i}$). Note that the local coordinate system (i) is obtained by rotating the local coordinate system (1) along the fiber direction ($\boldsymbol{v}$) by arbitrary degree (θ_i). (C) The six independent strain components in the local coordinate system (1). (D) illustration of ε_{xx}, γ_{xy}, and γ_{xz}, of which the latter two act in the yz plane. (E) Illustration of four tract-related strains that are parameters of interest in the current study, i.e., tract-oriented normal strain ε_a characterizes the normal strain along the fiber tract, tract-perpendicular normal strain ε_t characterizes the maximum normal strain perpendicular to the fiber tract, tract-oriented shear strain γ_a characterizes the shear strain along the fiber tract, and tract-perpendicular shear strain γ_t characterizes the maximum shear strain perpendicular to the fiber tract.

The presented method has been similarly used to compute the orientation-dependent strains in neural cells in *in vitro* models [60, 61, 63, 82]. We have previously used this method to estimate the tract-related deformation during *in silico* impact simulations, in which the real-time fiber orientation (i.e., the

deformed fiber orientation that changes at each timestep of the simulation) was used [83]. We acknowledge that is flawed and the undeformed fiber orientation should be used (e.g., the static first principal eigenvector of diffusion tensor used in the current study). We also clarify the mathematical derivation presented herein is exactly the same as those in our previous study [83], except that the correct orientation (i.e., the undeformed fiber orientation) as input to compute the tract-related strains. An erratum to our previous study [83] will be published separately.

Appendix B Influence of the disparity of voxel resolution on white matter tract-related strains

To assess how the difference in voxel resolutions (1.5 mm vs. 2.0 mm) affects the tract-related strains, strain tensor data from one randomly selected volunteer test with a spatial resolution of 1.5 mm is down-sampled to 2 mm using the nearest neighbouring method [44]. Both the original and down-sampled imaging data are used to calculate the tract-related strains (Fig B1). The similarity in strain contours and overlap in the percentile strain values between two resolutions indicate the spatial resolution disparity (i.e., 1.5 mm vs. 2.0 mm) has negligible effects on four maximum tract-related strains.

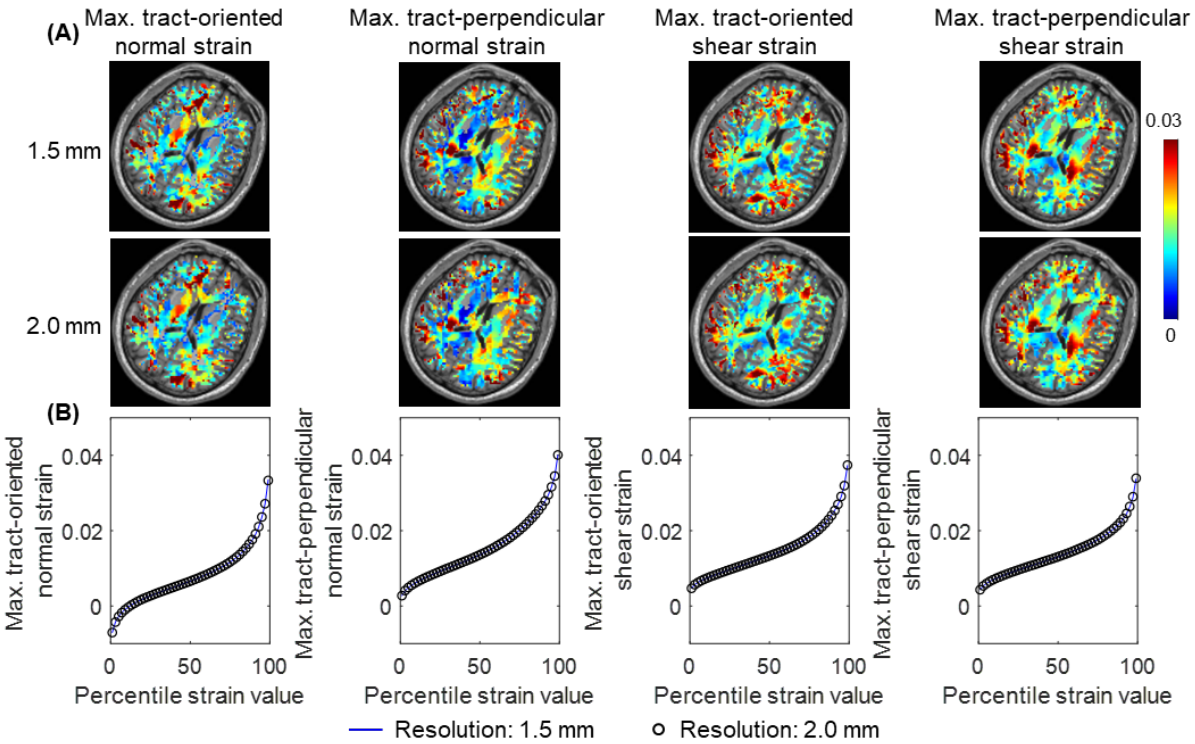

Fig B1. Influence of imaging down-sampling (from 1.5 mm to 2.0 mm) on the maximum values of four tract-related strains in terms of strain distribution (A) and percentile strain values (B).

Appendix C Comparisons of four tract-related strain peaks

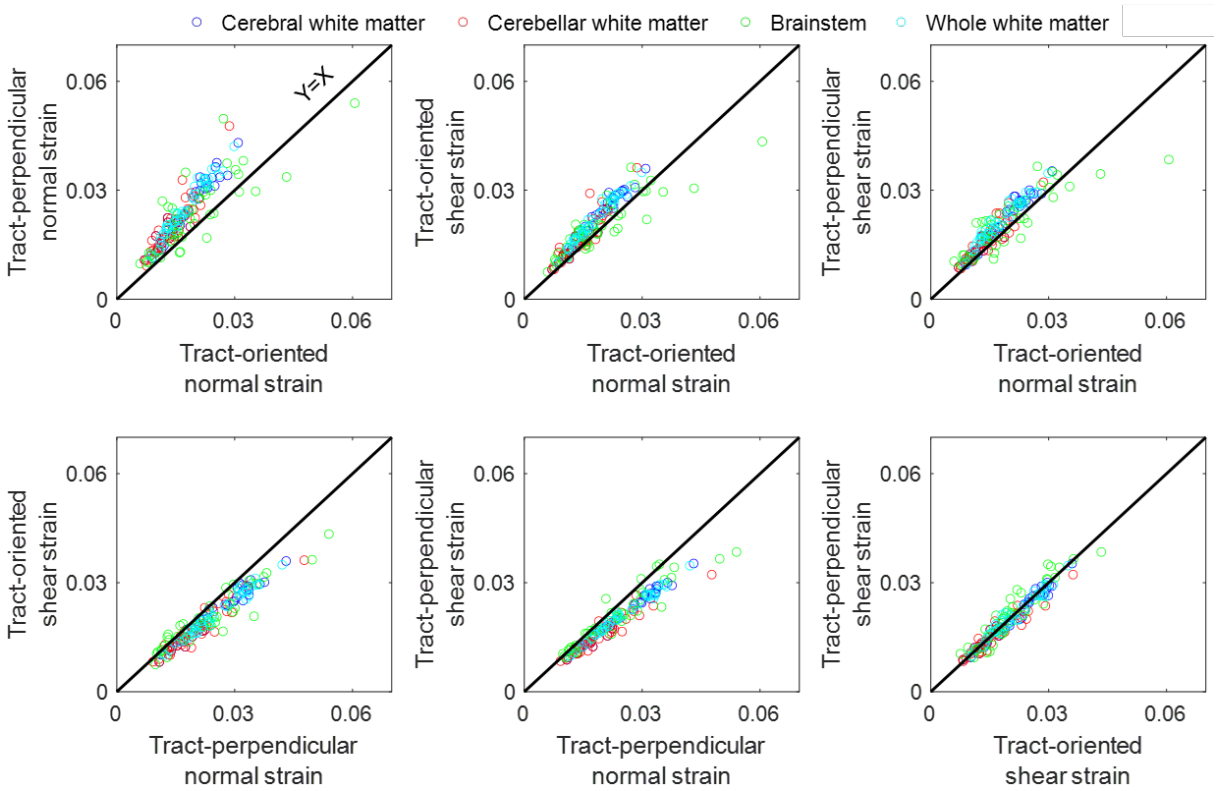

Fig C1. One-one comparisons of four tract-related strains peaks in the cerebral white matter, cerebellar white matter, brainstem, and whole white matter.

Appendix D Pearson's correlation between angular kinematics and tract-related strain peaks

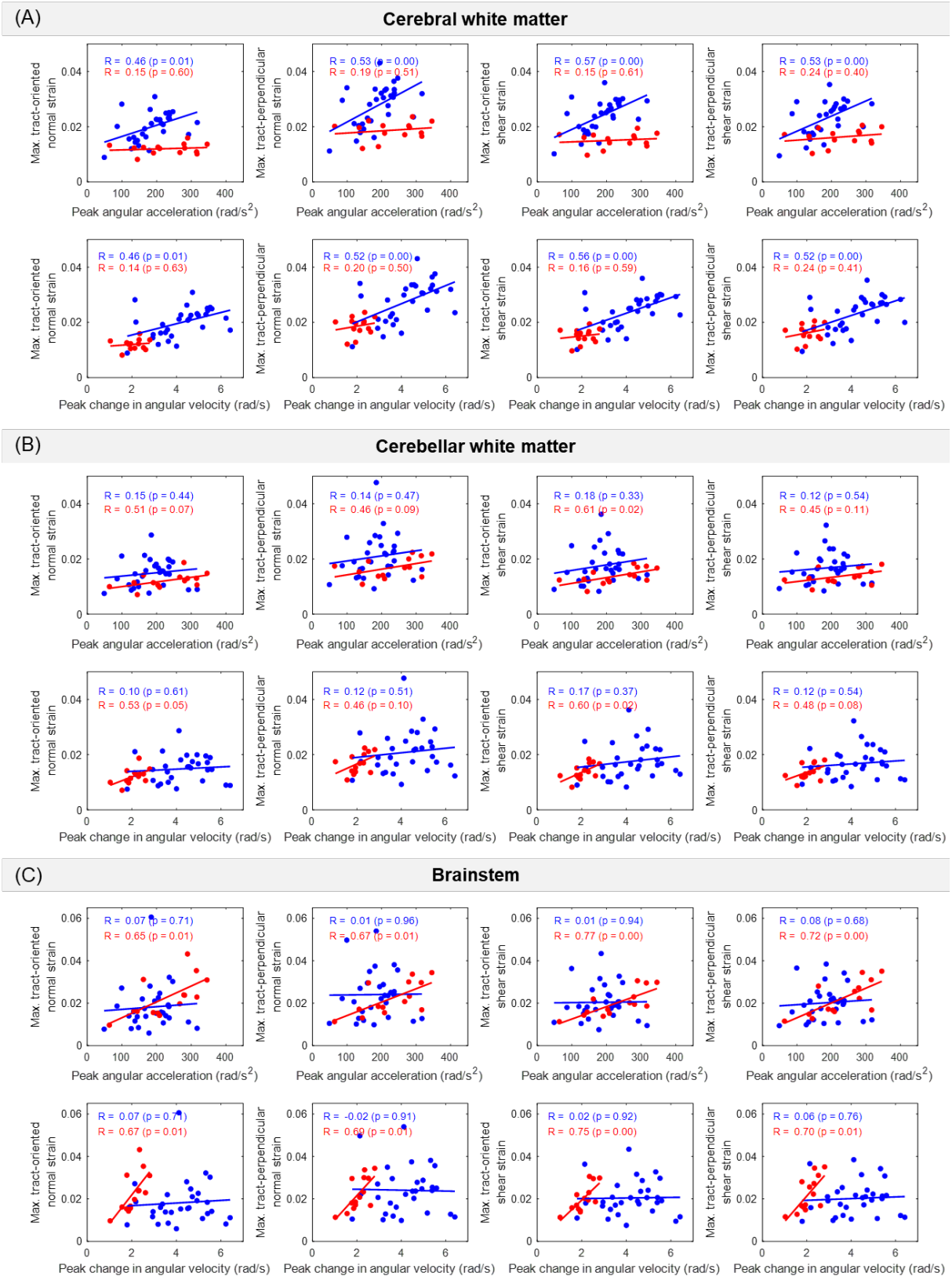
(A)
Cerebral white matter
R = 0.46 (p = 0.01)
R = 0.15 (p = 0.60)
R = 0.53 (p = 0.00)
R = 0.19 (p = 0.51)
R = 0.57 (p = 0.00)
R = 0.15 (p = 0.61)
R = 0.53 (p = 0.00)
R = 0.24 (p = 0.40)
R = 0.46 (p = 0.01)
R = 0.14 (p = 0.63)
R = 0.52 (p = 0.00)
R = 0.20 (p = 0.50)
R = 0.56 (p = 0.00)
R = 0.16 (p = 0.59)
R = 0.52 (p = 0.00)
R = 0.24 (p = 0.41)
(B)
Cerebellar white matter
R = 0.15 (p = 0.44)
R = 0.51 (p = 0.07)
R = 0.14 (p = 0.47)
R = 0.46 (p = 0.09)
R = 0.18 (p = 0.33)
R = 0.61 (p = 0.02)
R = 0.12 (p = 0.54)
R = 0.45 (p = 0.11)
R = 0.10 (p = 0.61)
R = 0.53 (p = 0.05)
R = 0.12 (p = 0.51)
R = 0.46 (p = 0.10)
R = 0.17 (p = 0.37)
R = 0.60 (p = 0.02)
R = 0.12 (p = 0.54)
R = 0.48 (p = 0.08)
(C)
Brainstem
R = 0.07 (p = 0.71)
R = 0.65 (p = 0.01)
R = 0.01 (p = 0.96)
R = 0.67 (p = 0.01)
R = 0.01 (p = 0.94)
R = 0.77 (p = 0.00)
R = 0.08 (p = 0.68)
R = 0.72 (p = 0.00)
R = 0.07 (p = 0.71)
R = 0.67 (p = 0.01)
R = -0.02 (p = 0.91)
R = 0.60 (p = 0.01)
R = 0.02 (p = 0.92)
R = 0.75 (p = 0.00)
R = 0.06 (p = 0.76)
R = 0.70 (p = 0.01)
Max. tract-oriented normal strain
Max. tract-perpendicular normal strain
Max. tract-oriented shear strain
Max. tract-perpendicular shear strain
Peak angular acceleration (rad/s^2)
Peak change in angular velocity (rad/s)

700

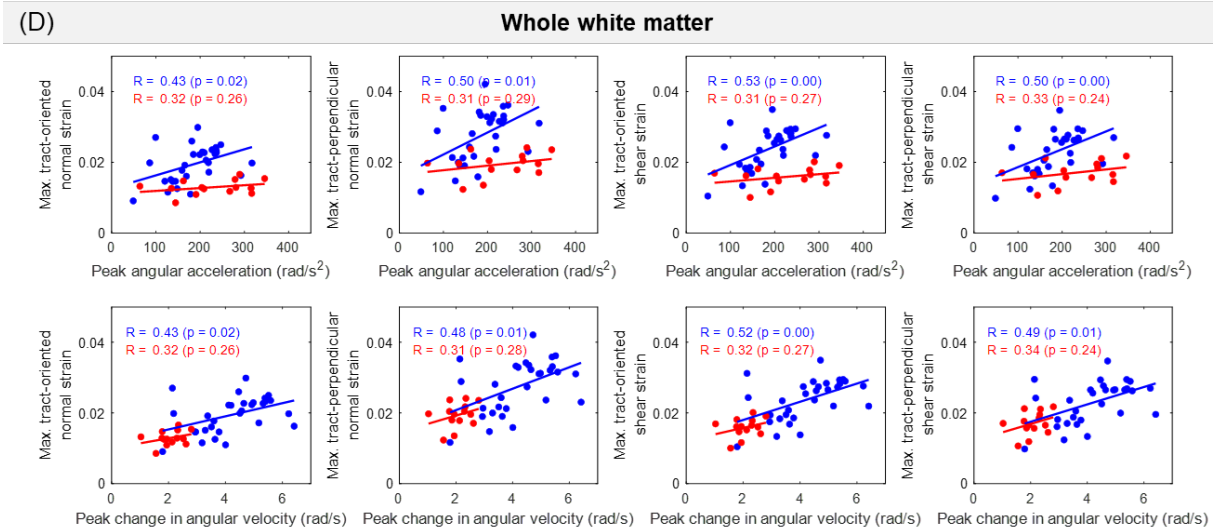

Fig D1. Person's correlations between peak angular kinematics (i.e., peak angular acceleration, peak change in angular velocity) and max. tract-related strains (95th percentile values) in cerebral white matter (A), cerebellar white matter (B), brainstem (C), and whole white matter (D) during neck rotation (blue) and neck extension (red).